Oxophilic Ce single atoms-triggered active sites reverse for superior alkaline hydrogen evolution

Kebin Zhou (kbzhou@ucas.ac.cn)
University of Chinese Academy of Sciences
Fengyi Shen
University of Chinese Academy of Sciences
Zhihao Zhang
National Engineering Laboratory for VOCs Pollution Control Material & Technology, Research Center for Environmental Material and Pollution Control Technology, University of Chinese Academy of Scienc
Zhe Wang
School of Chemical Sciences, University of Chinese Academy of Sciences
Hao Ren
Xinhu Liang
University of Chinese Academy of Sciences
Zengjian Cai
University of Chinese Academy of Sciences
Shitu Yang
University of Chinese Academy of Sciences
Guodong Sun
University of Chinese Academy of Sciences
yanan cao
Xiaoxin Yang
School of Chemical Sciences, University of Chinese Academy of Sciences
Mingzhen Hu
Tsinghua University
Zhengping Hao
University of Chinese Academy of Sciences (UCAS) https://orcid.org/0000-0003-0553-3626

Article

Keywords:

Posted Date: July 6th, 2023

DOI: https://doi.org/10.21203/rs.3.rs-3133914/v1

Additional Declarations: There is **NO** Competing Interest.

Version of Record: A version of this preprint was published at Nature Communications on January 10th, 2024. See the published version at https://doi.org/10.1038/s41467-024-44721-5.

Abstract

The state-of-the-art alkaline HER catalyst of united Ru single atoms and small Ru nanoparticles (Ru_1-Ru_n) has sparked considerable research interest. However, it remains a serious problem that hydrogen evolution primarily occurs on the less active Ru single atoms instead of the more efficient small Ru nanoparticles in Ru_1-Ru_n, hence largely falling short of its full activity potential and unnecessarily increasing Ru usage amount. Here, we report that combining oxophilic Ce single atoms and fully-exposed Ru nanoclusters on a N functionalized carbon (Ce_1-Ru_n/NC) can facilely reverse alkaline hydrogen evolution centers to the more active fully-exposed Ru nanoclusters driven by the strong oxophilicity of Ce and thus greatly improves HER activity as well as Ru atom efficiency. Remarkably, the Ce_1-Ru_n/NC outperformed all the other Ru-based alkaline HER catalysts to date by its excellent mass activity. This finding is expected to shed new light on developing more efficient and cost-saving alkaline HER catalyst.

Introduction

Hydrogen production via water electrolysis has been regarded one of the most promising approach to mediate the climate change and the global energy crisis.[1-2] In practice, hydrogen evolution reaction (HER) could proceed either in acid or alkaline electrolyte,[3] while industry preferred alkaline HER because of its favorable reaction kinetics for the sluggish anodic half-reaction of water-splitting and relatively lower cost.[4-6] However, the decrease of proton content in alkaline electrolyte drastically lowered HER activity of the commercial Pt electrocatalysts. About two orders of magnitude reduction in activity was commonly identified for the commercial Pt/C when used in alkaline electrolyte.[7] Moreover, in sharp contrast with the acid HER, hydrogen evolution in alkaline electrolyte underwent a unique Volmer step involving dissociation of H_2O (equation 1) and thus required extra energy to scissor the OH-H bond, which largely determined the overall reaction rate of alkaline HER.[8] To this end, promoting electrocatalytic water dissociation in alkaline electrolyte became of paramount importance to boost corresponding HER activity.

(1) $H_2O + e^- \rightarrow H_{ad} + OH^-$ (Volmer step)

(2) $H_2O + H_{ad} + e^- \rightarrow H_2 + OH^-$ (Heyrovsky step)

(3) $H_{ad} + H_{ad} \rightarrow H_2$ (Tafel step)

In the past decades, Ru has shown great potential to substitute the expensive Pt for alkaline HER by virtue of its relatively lower Gibbs free energy barrier for water dissociation and reduced metal price.[9-10] To maximize Ru metal efficiency, Ru single atom catalysts were employed to electro-catalyze the alkaline HER.[11-13] Nevertheless, the Ru single atoms exhibited very low reactivity for water dissociation because of its substantial uphill energy for breaking the OH-H bond, hence significantly impeding its alkaline HER activity.[9]

Most recently, a united catalyst of Ru single atoms and small Ru nanoparticles (Ru_1-Ru_n) has attracted tremendous research interest because of its enhanced alkaline HER activity.[14-17] Theoretical calculations unveiled that water molecules could be facilely dissociated on Ru_1-Ru_n catalyst with a quite low Gibbs free energy barrier, which greatly compensated the energy-requiring Volmer step of alkaline HER and accelerated the reaction kinetics.[18-20] After water dissociation, the produced H was adsorbed on Ru single atoms for further hydrogen evolution while the produced OH was firstly bonded with small Ru nanoparticles and then desorbed in the form of OH^- as illustrated in **Scheme 1**. However, it was evident that the small Ru nanoparticles of the Ru_1-Ru_n catalyst merely took part in water dissociation and OH^- desorption during the alkaline HER and large numbers of Ru sites therein just acted as spectators of hydrogen evolution. What was more, the Ru single atoms were less active to produce hydrogen than the small Ru nanoparticles in view of their different H binding strength.[21-22] As a result, excessive Ru was unnecessarily used in the Ru_1-Ru_n catalyst to attain high alkaline HER activity, leading to a great waste of the precious Ru metal. One can expect that enhanced alkaline HER activity and Ru atom efficiency would be possibly acquired if reversing the hydrogen evolution centers of the Ru_1-Ru_n catalyst from the single atom sites to the more active small Ru nanoparticles, which is urgently awaited to be explored.

Herein, we report that by uniting oxophilic Ce single atoms and fully-exposed Ru nanoclusters on a N functionalized carbon support, the alkaline hydrogen evolution centers were facilely reversed to the more efficient Ru nanoclusters. The driving force for the active site reverse was the strong oxophilicity of Ce through which the OH obtained by water dissociation was selectively bonded with the Ce single atoms while the H was moderately adsorbed on the fully-exposed Ru nanoclusters for more efficient hydrogen evolution (**Scheme 1**). Furthermore, water dissociation was also significantly promoted benefiting from the strong synergies between the oxophilic Ce single atoms and the fully-exposed Ru nanoclusters. As such, improved alkaline HER activity and maximized Ru atom efficiency were simultaneously attained over the Ce_1-Ru_n/NC catalyst, providing a new avenue to more cost-effective alkaline HER.

Results

Synthesis and characterization of the Ce_1-Ru_n/NC. The united catalyst of oxophilic Ce single atoms and fully-exposed small Ru nanoclusters was prepared on a N functionalized XC-72 carbon support (indicated as Ce_1-Ru_n/NC, see Figure S1-2 for details). As a control, pure Ru nanoclusters and Ce single atoms were also prepared on the NC support (denoted as Ru_n/NC and Ce_1/NC, respectively) using a similar method. The loading amount of Ce in Ce_1/NC (Fig. 1a) was measured to be 0.03wt.% by an inductively coupled plasma optical emission spectrometer (ICP-OES). Due to the low Ce loadings, only the broad X-ray diffraction (XRD) peaks of carbon support[23] were observed for the Ce_1/NC as displayed in Figure S3. In addition, the high-angle annular dark-field scanning transmission electron microscopy (HAADF-STEM) images of the Ce_1/NC in Figure S4-6 excluded any particles in it. It was further unveiled by the aberration-corrected HAADF-STEM (AC HAADF-STEM) measurement that Ce species were atomically dispersed in

Ce_1/NC (Fig. 1b-d) and corresponding energy-dispersive X-ray spectrometry (EDS) elementary mapping images in Fig. 1e-g also confirmed the uniform Ce dispersion.

Likewise, we have characterized the Ru_n/NC (Fig. 1h) and the Ce_1-Ru_n/NC (Fig. 1o) via the microscopic techniques. As presented by the AC HAADF-STEM images of the Ru_n/NC in Fig. 1i-j, fully-exposed Ru nanoclusters with an average particle size of 1.1 ± 0.3 nm were evenly dispersed on the NC support. The EDS elementary mapping images of a small nanocluster in Ru_n/NC (Fig. 1k-n) revealed its Ru element nature. The AC HAADF-STEM images of the Ce_1-Ru_n/NC in Fig. 1p-q showed that the mean particle size of the fully-exposed Ru nanoclusters in it was 1.0 ± 0.2 nm. Meanwhile, Ce species were atomically dispersed around the fully-exposed Ru nanoclusters. Corresponding EDS elementary mapping images in Fig. 1r-u also indicated uniform dispersion of the fully-exposed Ru nanoclusters and the Ce single atoms in Ce_1-Ru_n/NC. No diffraction peaks of Ru were identified for the Ru_n/NC and the Ce_1-Ru_n/NC as shown in Figure S7 because of their ultrasmall Ru nanoclusters. The Ru loading amounts of the Ce_1-Ru_n/NC and the Ru_n/NC were both 1wt.% while the Ce weight loading in Ce_1-Ru_n/NC was 0.03wt.% as determined by the ICP-OES measurements.

The coordination environment of Ru and Ce in Ce_1/NC, Ru_n/NC and Ce_1-Ru_n/NC was further examined by the X-ray absorption fine-structure (XAFS) measurement. Figure 2a showed the near-edge XAFS spectra (XANES) at Ru K-edge of the Ce_1-Ru_n/NC, Ru_n/NC and reference Ru foil and RuO_2. It was displayed by the enlarged Ru K-edge XANES spectra in the inset of Fig. 2a that the edge absorption energies of Ce_1-Ru_n/NC and Ru_n/NC were between Ru foil and RuO_2, which demonstrated the oxidation state of the fully-exposed Ru nanoclusters in Ce_1-Ru_n/NC and Ru_n/NC was between 0 and + 4. The formation of positively charged Ru nanoclusters in Ce_1-Ru_n/NC and Ru_n/NC was due to the strong N-Ru coordination through which Ru electrons could be easily transferred to connecting N of much larger electronegativity than Ru[24], hence leading to the increase of oxidation state of Ru nanoclusters of them. The edge energy of the Ce_1-Ru_n/NC showed an obvious negative shift relative to the Ru_n/NC and thus an enhancement of its Ru electron density,[25–26] which possibly derived from Ce electron donation. To check this assumption, the Bader charge analysis were further conducted. It was demonstrated in Figure S8 that electrons could be facilely transferred from Ce to Ru with a net electron transfer number of 0.05, which agreed well with the XANES data.

The Fourier transforms of the Ru K-edge extended XAFS (EXAFS) oscillations in the R space of the Ce_1-Ru_n/NC and the Ru_n/NC in Fig. 2b presented a main coordination peak below 2 Å, matching to the Ru-N coordination.[27] The Ru-Ru coordination peak at about 2.7 Å was also identified for both of the Ce_1-Ru_n/NC and the Ru_n/NC. However, the peak intensity of Ru-Ru coordination was largely reduced relative to Ru-N coordination, implying their significant difference in coordination numbers.[28] The EXAFS data fitting of the Ce_1-Ru_n/NC and the Ru_n/NC in Fig. 2c-d and Figure S9-10 then provided the exact Ru-Ru and Ru-N coordination information of them. As summarized in Table S1, the Ru-N coordination ratio was largely increased compared with the Ru-Ru coordination both for the Ce_1-Ru_n/NC and the Ru_n/NC. The

enhanced Ru-N coordination ratio was a feature for N-stabilized small Ru nanoclusters because the particle downsizing of Ru significantly decoupled the Ru-Ru bond and strengthened the Ru-N coordination.[26] This result was also supported by the EXAFS wavelet transform (WT) results. As displayed in Fig. 2e, the Ru-N coordination intensity was obviously stronger than the Ru-Ru coordination both for the Ce_1-Ru_n/NC and the Ru_n/NC. The Ce L_{III}-edge XANES and EXAFS spectra of the Ce_1-Ru_n/NC in Fig. 2f-g and Figure S11-13 again confirmed the single atom nature of Ce in Ce_1-Ru_n/NC, which was consistent with the above AC HAADF-STEM observation. In addition, the electron transfer between Ce single atoms and Ru nanoclusters in Ce_1-Ru_n/NC was further evidenced by the Ru 3p XPS spectra in Fig. 2h, where the Ru^0 binding energy peak of the Ce_1-Ru_n/NC was slightly negatively shifted compared with the Ru_n/NC because of the electron back-donation from Ce to Ru.

Electrocatalytic evaluations for alkaline HER. According to reported findings,[29] water dissociation on the surface of catalyst was largely dependent on corresponding OH adsorption strength. Strong OH binding was beneficial to water molecules' polarization and elongation and commonly promoted water dissociation. Thus, we have firstly conducted the cyclic voltammetry (CV) measurements in 1.0 M KOH solution to explore the OH adsorption strength on the Ru_n/NC and the Ce_1-Ru_n/NC catalysts, respectively, before electrochemical alkaline HER evaluations. Figure 3a displayed that the OH-adsorption peak intensity around 0.60 to 1.00 V[30] of the Ce_1-Ru_n/NC was much stronger than the Ru_n/NC, indicating intensified OH adsorption on the Ce_1-Ru_n/NC over the Ru_n/NC thanks to Ce single atoms promoting. As a control, we have also prepared a CeO_2 nanoparticle integrated Ru_n catalyst on NC support (Ru_n-CeO_2/NC, Figure S14-18) with similar Ru nanoclusters to Ru_n/NC and Ce_1-Ru_n/NC while the Ce sites therein were bonded with O. It was found that the OH-adsorption peak intensity of the Ru_n-CeO_2/NC was markedly decreased relative to the Ce_1-Ru_n/NC due to the O blocking of Ce sites. These results indicated that OH was prone to bond with Ce single atoms of the Ce_1-Ru_n/NC catalyst as vividly depicted in Fig. 3b.

To further confirm this, we have performed the *in situ* Raman measurements in 1.0 M KOH electrolyte under real alkaline HER conditions (Figure S19). As presented in Fig. 3c, the Raman vibration peaks at 1533 cm^{-1} and 1390 cm^{-1} of the Ce_1-Ru_n/NC catalyst were gradually intensified with the increase of reaction potentials during alkaline HER. By contrast, the Ru_n/NC catalyst merely showed the vibration peaks for the D band and G band of carbon support (Fig. 3d) under the same testing conditions.[31] Since there was no record of the two Raman vibration peaks of the Ce_1-Ru_n/NC catalyst at 1533 cm^{-1} and 1390 cm^{-1}, we have further conducted the theoretical simulations. Through theoretical fitting of the Raman spectrum of the Ce_1-Ru_n/NC catalyst before alkaline HER test (Fig. 3e), we found that the Raman vibration peaks at 1533 cm^{-1} and 1390 cm^{-1} were assigned to the Ce-N stretching vibration but the two peaks were very weak before alkaline HER test. Thus, it was reasonable to assume that the strengthening of the Raman vibration peaks at 1533 cm^{-1} and 1390 cm^{-1} was related to OH or H produced during the alkaline HER process. To this end, we have examined both OH and H effects on the Ce-N stretching vibration. Strikingly, upon introducing OH to the Ce-N sites of the Ce_1-Ru_n/NC catalyst, corresponding

Raman peak intensities at 1533 cm^{-1} and 1390 cm^{-1} were significantly strengthened as shown in Fig. 3f, agreeing well with the *in situ* Raman spectra in Fig. 3b. By contrast, it was manifested in Figure S20 that H had a negligible impact on intensifying the Ce-N stretching vibration at these positions. Evidently, OH was more susceptible to bond with the Ce single atoms in Ce_1-Ru_n/NC during alkaline HER and in turn made the fully-exposed Ru nanoclusters therein serve as hydrogen evolution centers, hence realizing the active site reverse relative to the Ru_1-Ru_n catalyst.

The Ce_1-Ru_n/NC and other control catalysts were then employed for electrochemical alkaline HER evaluations. As expected, the Ce_1-Ru_n/NC exhibited much enhanced catalytic activity than other catalysts as indicated by their linear sweep voltammetry (LSV) curves in Fig. 4a. To make it clear, the current density of the Ce_1-Ru_n/NC at − 0.05 V was up to 30 mA cm^{-2}, which was 2.3 times and 4.6 times that of the 20wt.% Pt/C and the Ru_n/NC as demonstrated in Fig. 4b. When the reaction potential reached − 0.15 V, the current density of the Ce_1-Ru_n/NC was much improved to 281 mA cm^{-2} and became 3.5 times that of the 20wt.% Pt/C and 8.5 times that of the Ru_n/NC. Moreover, the mass activity of the Ce_1-Ru_n/NC was even larger than the 20wt.% Pt/C as shown in Figure S21. Figure 4c disclosed that the Tafel slope of the Ce_1-Ru_n/NC was the lowest among these catalysts, thus endowing the Ce_1-Ru_n/NC with fast reaction kinetics for hydrogen evolution. Additionally, the smallest charge transfer resistance (R_{ct}) of the Ce_1-Ru/NC as shown in Figure S22 provided further evidence for its rapid HER kinetics. To examine the intrinsic activity of these catalysts, we have conducted the turnover frequency (TOF) measurements in the potential range from − 0.01 V to − 0.06 V. It was found that the TOF values of the Ce_1-Ru_n/NC and the Ru_n/NC were obviously higher than the 20wt.% Pt/C as shown in Fig. 4d. Moreover, with the assistance of Ce single atoms, the TOF value of the Ce_1-Ru_n/NC was significantly larger than the Ru_n/NC. By contrast, the Ru_n-CeO_2/NC showed obviously reduced TOF value with respect to the Ce_1-Ru_n/NC, which possibly derived from its weak OH adsorption strength as demonstrated by the aforementioned CV results in Fig. 3a.

Figure 4e and Figure S23 presented a comparison of the alkaline HER mass activity between the Ce_1-Ru_n/NC and other reported Ru-based catalysts. Obviously, the Ce_1-Ru_n/NC catalyst outperformed all the Ru-based alkaline HER catalysts to date to the best of our knowledge in terms of mass activity both at − 0.05 V and − 0.1 V (corresponding data were also provided in Table S2 and S3). Stability measurement of alkaline HER was commonly conducted at the current density of 10 mA cm^{-2} to fulfill the requirement of electrochemical performance at a device level.[32] However, the current density should be no less than 100 mA cm^{-2} in order to meet the commercial standard for industrial alkaline HER.[33] Therefore, we have measured the catalytic stability of the Ce_1-Ru_n/NC and the commercial 20wt.% Pt/C at a high current density of 150 mA cm^{-2}. As demonstrated in Fig. 4f, the Ce_1-Ru_n/NC catalyst displayed excellent catalytic stability for 100 hours at such high current density while the 20wt.% Pt/C showed obvious catalytic stability degrading in less than 3 hours, displaying great potential of the Ce_1-Ru_n/NC catalyst for practical applications.

Theoretical investigations for the Ce_1-Ru_n/NC catalyst's superior alkaline HER activity. The first-principle density functional theory (DFT) calculations with spin-polarization were further carried out to explore the origin of the excellent alkaline HER activity of the Ce_1-Ru_n/NC catalyst. The structural models of the Ce_1-Ru_n/NC, Ru_n/NC and Ce_1/NC were built based on the EXAFS fitting data, wherein Ce single atom was coordinated with six N atoms and Ru nanocluster was stabilized by four N atoms on the NC support. All the structure details and model files of the Ce_1-Ru_n/NC, Ru_n/NC and Ce_1/NC catalysts were provided in supporting information (Figure S24-26). It was found that the Ce_1/NC showed a huge Gibbs free energy barrier for water dissociation as displayed in Figure S27-28, which explained its low reactivity for the alkaline HER (Fig. 4a). Figure 5a showed that the Ce_1-Ru_n/NC catalyst possessed a micro-electric field due to the notable difference in the electrostatic potential distribution between Ce single atoms and fully-exposed Ru nanoclusters. Consequently, the polarized water molecules could be easily elongated upon contacting the Ce_1-Ru_n/NC catalyst. Notably, the O-H bond of water was significantly elongated from 0.98 Å to 1.04 Å when adsorbed on the Ce_1-Ru_n/NC catalyst, hence efficiently favoring water activation.

In theory, water had two possible activation patterns on the Ce_1-Ru_n/NC catalyst: i) the OH groups bond with Ce single atoms while the H atoms bond with Ru nanoclusters (Ce_1OH-Ru_nH route); and ii) the H atoms bond with Ce single atoms while the OH groups bond with Ru nanoclusters (Ce_1H-Ru_nOH route). Therefore, we have performed DFT calculations for both routes. As displayed in Fig. 5b, the Ce_1H-Ru_nOH route was endothermic by 0.6 eV while the Ce_1OH-Ru_nH route was particularly exothermic by 4.5 eV. The sharply different thermodynamics of the Ce_1H-Ru_nOH route and the Ce_1OH-Ru_nH route was most likely derived from the distinct oxophilicity of Ru and Ce. Compared with the d-block Ru, the f-block Ce was much more oxophilic[34] by means of which Ce was more prone to bond with OH instead of H, hence making the Ce_1OH-Ru_nH route more thermodynamically preferred.

As far as the Ce_1-Ru_n/NC and the Ru_n/NC were concerned, the exothermic energy of the Ce_1-Ru_n/NC (4.5 eV, Ce_1OH-Ru_nH route) was 9 times that of the Ru_n/NC (0.5 eV) in water activation process, revealing the Ce_1-Ru_n/NC was more thermodynamically favorable to dissociate water than the Ru_n/NC. Besides, the Gibbs free energy barriers for breaking OH-H bond of water over the Ce_1-Ru_n/NC catalyst was also lower than the Ru_n/NC. Therefore, the Ce_1-Ru_n/NC catalyst was both thermodynamically and kinetically beneficial to promote water dissociation. After water dissociation, OH was energetically bonded with the oxophilic Ce single atoms while H was adsorbed on the fully-exposed Ru nanoclusters. To gain insight into the hydrogen formation and the OH^- desorption over the Ce_1-Ru_n/NC and the Ru_n/NC catalysts, we have further carried out calculations for H binding strength (ΔG_{H*}) and OH^- desorption energy barriers of them.

Because of the electron enriching of Ru in the Ce_1-Ru_n/NC compared with the Ru_n/NC as revealed by the aforementioned XANES and XPS results, the calculated d-band center of Ru in the Ce_1-Ru_n/NC (−1.48 eV) displayed an obvious downshift compared with the Ru_n/NC (−1.43 eV) as shown in Fig. 5c and **d**.

According to previous reports,[29] the low reactivity of Ru metal toward HER was usually ascribed to its too strong H adsorption that hindered H transfer and H_2 formation. The Ru d-band center downshift of the Ce_1-Ru_n/NC would facilely weaken H binding strength[35] to enable more facile H transfer. As shown in Fig. 5e, the ΔG_{H^*} of the Ce_1-Ru_n/NC was obviously closer to the optimum than the Ru_n/NC, which made the Ce_1-Ru_n/NC more efficient for hydrogen evolution. Furthermore, the electron localization function (ELF) analysis (inset of Fig. 5e) disclosed that a weaker degree of electron localization in the Ru-H bonding region was identified for the Ce_1-Ru_n/NC than the Ru_n/NC, thus weakening the hydrogen binding strength thereon for more favorable hydrogen production. On the other hand, the OH^- desorption from the Ce_1-Ru_n/NC was also greatly favored compared with the Ru_n/NC in view of its lower OH^- desorption energy barrier (1.0 eV) as indicated in Fig. 5b.

In conclusion, we report a united catalyst of oxophilic Ce single atoms and fully-exposed Ru nanoclusters on a N functionalized carbon support that facilely reverses the hydrogen evolution centers to the more efficient Ru nanoclusters during alkaline HER, hence attaining significantly improved HER activity and Ru atom efficiency. Notably, the mass activity of the Ce_1-Ru_n/NC surpassed all the Ru-based alkaline HER catalysts to date, coupled with excellent durability. Extensive experiment data and theoretical calculations well confirmed the active site reverse over the Ce_1-Ru_n/NC catalyst for more efficient alkaline hydrogen evolution. This unexpected finding possibly provides new insights into designing more cost-effective alkaline HER catalyst.

Methods

Materials. All chemicals were of analytical grade and used as received without further purification. Ruthenium chloride and urea were purchased from Macklin Biochemical Co., Ltd. Urea and carbon support (XC-72) were obtained from the Aladdin Biochemical Technology Co., Ltd. Cerium nitrate hexahydrate were purchased from the Sinopharm Chemical Reagent Co., Ltd. The 20% commercial Pt/C catalysts were purchased from the Sigma-Aldrich. The Nafion PFSA Polymer with 5% polymer content was acquired from the DuPont company. Ethanol was obtained from the Tongguang Fine Chemical Company Beijing. Hydrophilic carbon paper was purchased from the Kelude Experimental Equipment Technology Co., Ltd.

Preparation of N functionalized carbon support (NC). The N functionalized carbon supports were prepared according to our previous reports.[36–37] Typically, 2 g of XC-72 carbon was homogeneously grinded with 3 g of urea. After which, the mixture was calcined at 150°C for 2 hours and 300°C for another 4 h in a fully sealed crucible. The product was then washed sufficiently with water and dried at 60 ^oC overnight.

Synthesis of the CeO_2/NC. The preparation of CeO_2/NC was prepared via the impregnation method. To make it clear, 6 mg of $Ce(NO_3)_3{\cdot}6H_2O$ were firstly added to 20 mL of deionized water and stirred to dissolve the Ce precursor. Subsequently, 0.1 g of NC support were added to the above solution. After

further stirring for 12 h, the mixture was centrifugated and washed thoroughly, and the obtained solid products were dried at 60°C overnight. At last, the obtained powders were reduced with hydrogen at 700°C for 2 hours.

Preparation of the Ce_1/NC. The prepared CeO_2/NC was then allowed for acid treatment (pH = 1) overnight. After sufficient washing and centrifugation, the obtained solid products were dried at 60°C overnight to make the Ce_1/NC catalyst.

Preparation details of the Ce_1-Ru_n/NC. Firstly, 2.5 mg of $RuCl_3$ were dissolved in 10 mL of deionized water. After which, 0.05 g of Ce_1/NC was added to the $RuCl_3$ solution under mild stirring. After stirring for another 12 h, the mixture was sufficiently washed, and the obtained solid products were collected and dried at 60°C overnight. Finally, the obtained powders were reduced at 250°C for 2 hours under hydrogen atmosphere.

Synthetic method of the Ru_n/NC. To begin with, 2.5 mg of $RuCl_3$ were added to 10 mL of deionized water and stirred to totally dissolve the Ru precursors. After which, 0.05 g of NC support were added to the $RuCl_3$ solution under mild stirring. After further stirring for 12 hours, the mixture was sufficiently centrifugated and washed. The obtained solid powders were collected and dried at 60°C overnight. At last, the obtained powders were reduced with hydrogen at 250°C for 2 hours.

Preparation of the Ru_n-CeO_2/NC. The preparation of the Ru_n-CeO_2/NC was as follows: 2.5 mg of $RuCl_3$ were firstly added to 10 mL of deionized water under mild stirring. Subsequently, 0.05 g of CeO_2/NC was added to the $RuCl_3$ solution under stirring. After stirring for another 12 hours, the mixture was thoroughly centrifugated and washed. The acquired solid products were then collected and dried at 60°C overnight. After which, the obtained powders were reduced with hydrogen at 250°C for 2 hours.

Declarations

Acknowledgements

This work was supported by the National Natural Science Foundation of China (22072153, 22102185), Chinese Academy of Sciences and the Fundamental Research Funds for the Central Universities (E1E40310), National Key Research and Development Program of China (2022YFB3504200).

Author contributions

K.Z. and M.H. conceived the project. F.S., Z.W., H.R., X.L., Z.C., S.Y. prepared the catalysts and performed the characterizations. F.S., Z.W., H.R., G.S, Y.C. conducted the catalytic measurements. Z.Z. carried out the DFT calculations and Z.H. helped with the experiment analysis. All authors discussed the results and co-wrote the paper.

Competing interests

The authors declare no competing interests.

Additional information

Supplementary Information accompanies this paper at http://www.nature.com

Correspondence and requests for materials should be addressed to M.H., Z.H. or

K.Z.

Reprints and permission information is available at www.nature.com/reprints.

References

1. Chu, S., et al., Opportunities and challenges for a sustainable energy future. Nature 2012, *488*, 294–303.
2. Turner, J. A., Sustainable Hydrogen Production. Science 2004, *305*, 972–974.
3. Carmo, M., et al., A comprehensive review on PEM water electrolysis. Int. J. Hydrogen Energy 2013, *38*, 4901–4934.
4. Ursua, A., et al., Hydrogen Production From Water Electrolysis: Current Status and Future Trends. *Proc. IEEE* 2012, *100*, 410–426.
5. Yu, Z.-Y., et al., Clean and Affordable Hydrogen Fuel from Alkaline Water Splitting: Past, Recent Progress, and Future Prospects. Adv. Mater. 2021, *33*, 2007100.
6. Hu, C., et al., Recent progress made in the mechanism comprehension and design of electrocatalysts for alkaline water splitting. Energy Environ. Sci. 2019, *12*, 2620–2645.
7. Zhou, K. L., et al., Platinum single-atom catalyst coupled with transition metal/metal oxide heterostructure for accelerating alkaline hydrogen evolution reaction. Nat. Commun. 2021, *12*, 3783.
8. Jiang, W.-J., et al., Synergistic Modulation of Non-Precious-Metal Electrocatalysts for Advanced Water Splitting. Acc. Chem. Res. 2020, *53*, 1111–1123.
9. Hu, Q., et al., Subnanometric Ru clusters with upshifted D band center improve performance for alkaline hydrogen evolution reaction. Nat. Commun. 2022, *13*, 3958.
10. Mao, J., et al., Accelerating water dissociation kinetics by isolating cobalt atoms into ruthenium lattice. Nat. Commun. 2018, *9*, 4958.
11. Yang, J., et al., Efficient and Robust Hydrogen Evolution: Phosphorus Nitride Imide Nanotubes as Supports for Anchoring Single Ruthenium Sites. Angew. Chem., Int. Ed. 2018, *57*, 9495–9500.
12. He, Q., et al., Achieving Efficient Alkaline Hydrogen Evolution Reaction over a Ni5P4 Catalyst Incorporating Single-Atomic Ru Sites. Adv. Mater. 2020, *32*, 1906972.
13. Li, H., et al., A small change in the local atomic environment for a big improvement in single-atom catalysis. J. Mater. Chem. A 2021, *9*, 4184–4192.

14. He, Q., et al., Synergic Reaction Kinetics over Adjacent Ruthenium Sites for Superb Hydrogen Generation in Alkaline Media. Adv. Mater. 2022, *34*, 2110604.
15. Lu, B., et al., Ruthenium atomically dispersed in carbon outperforms platinum toward hydrogen evolution in alkaline media. Nat. Commun. 2019, *10*, 631.
16. Feng, Y., et al., Spherical vs. planar: Steering the electronic communication between Ru nanoparticle and single atom to boost the electrocatalytic hydrogen evolution activity both in acid and alkaline. Appl. Catal., B 2022, *307*, 121193.
17. Li, Y., et al., Ru single atoms and nanoclusters on highly porous N-doped carbon as a hydrogen evolution catalyst in alkaline solutions with ultrahigh mass activity and turnover frequency. J. Mater. Chem. A 2021, *9*, 12196–12202.
18. Tiwari, J. N., et al., High-Performance Hydrogen Evolution by Ru Single Atoms and Nitrided-Ru Nanoparticles Implanted on N-Doped Graphitic Sheet. Adv. Energy Mater. 2019, *9*, 1900931.
19. Cao, D., et al., Construction of Dual-Site Atomically Dispersed Electrocatalysts with Ru-C5 Single Atoms and Ru-O4 Nanoclusters for Accelerated Alkali Hydrogen Evolution. Small 2021, *17*, 2101163.
20. Zhang, L., et al., Exploring the Dominant Role of Atomic- and Nano-Ruthenium as Active Sites for Hydrogen Evolution Reaction in Both Acidic and Alkaline Media. Adv. Sci. 2021, *8*, 2004516.
21. Zhu, Y., et al., Supported Ruthenium Single-Atom and Clustered Catalysts Outperform Benchmark Pt for Alkaline Hydrogen Evolution. *Adv. Mater.* 2023, *DOI: 10.1002/adma.202301133.*
22. Wang, D., et al., Nickel metaphosphate supported ruthenium for all pH hydrogen evolution: From single atom, cluster to nanoparticle. Appl. Catal., B 2023, *325*, 122331.
23. Chen, Y., et al., Isolated Single Iron Atoms Anchored on N-Doped Porous Carbon as an Efficient Electrocatalyst for the Oxygen Reduction Reaction. Angew. Chem. Int. Ed. 2017, *56*, 6937–6941.
24. Atkins, P., et al., *Physical chemistry*. Macmillan: 2006; Vol. 1.
25. Pang, B., et al., Laser-assisted high-performance PtRu alloy for pH-universal hydrogen evolution. Energy Environ. Sci. 2022, *15*, 102–108.
26. Liang, Q., et al., Superassembly of Surface-Enriched Ru Nanoclusters from Trapping–Bonding Strategy for Efficient Hydrogen Evolution. ACS Nano 2022, *16*, 7993–8004.
27. Yu, J., et al., Tailoring the ruthenium reactive sites on N doped molybdenum carbide nanosheets via the anti-Ostwald ripening as efficient electrocatalyst for hydrogen evolution reaction in alkaline media. Appl. Catal., B 2020, *277*, 119236.
28. Beale, A. M., et al., EXAFS as a tool to interrogate the size and shape of mono and bimetallic catalyst nanoparticles. Phys. Chem. Chem. Phys. 2010, *12*, 5562–5574.
29. Zheng, Y., et al., The Hydrogen Evolution Reaction in Alkaline Solution: From Theory, Single Crystal Models, to Practical Electrocatalysts. Angew. Chem. Int. Ed. 2018, *57*, 7568–7579.
30. Zhang, J., et al., Competitive Adsorption: Reducing the Poisoning Effect of Adsorbed Hydroxyl on Ru Single-Atom Site with SnO2 for Efficient Hydrogen Evolution. Angew. Chem. Int. Ed. 2022, *61*, e202209486.

31. Wang, Y., et al., Raman spectroscopy of carbon materials: structural basis of observed spectra. Chem. Mater. 1990, *2*, 557–563.
32. Wei, C., et al., The Comprehensive Understanding of as an Evaluation Parameter for Electrochemical Water Splitting. Small Methods 2018, *2*, 1800168.
33. Fan, J., et al., Hydrogen Stabilized RhPdH 2D Bimetallene Nanosheets for Efficient Alkaline Hydrogen Evolution. J. Am. Chem. Soc. 2020, *142*, 3645–3651.
34. Kepp, K. P., A Quantitative Scale of Oxophilicity and Thiophilicity. Inorg. Chem. 2016, *55*, 9461–9470.
35. Nørskov, J. K., et al., Density functional theory in surface chemistry and catalysis. *Proc. Natl. Acad. Sci.* 2011, *108*, 937–943.
36. Hu, M., et al., Surface-Confined Synthesis of Ultrafine Pt-Rare Earth Nanoalloys on N-Functionalized Supports. Adv. Funct. Mater. 2022, *32*, 2202675.
37. Hu, M., et al., Direct Growth of Uniform Bimetallic Core-Shell or Intermetallic Nanoparticles on Carbon via a Surface-Confinement Strategy for Electrochemical Hydrogen Evolution Reaction. Adv. Funct. Mater. 2023, *33*, 2212097.

Scheme

Scheme 1 is available in the Supplementary Files section.

Figures

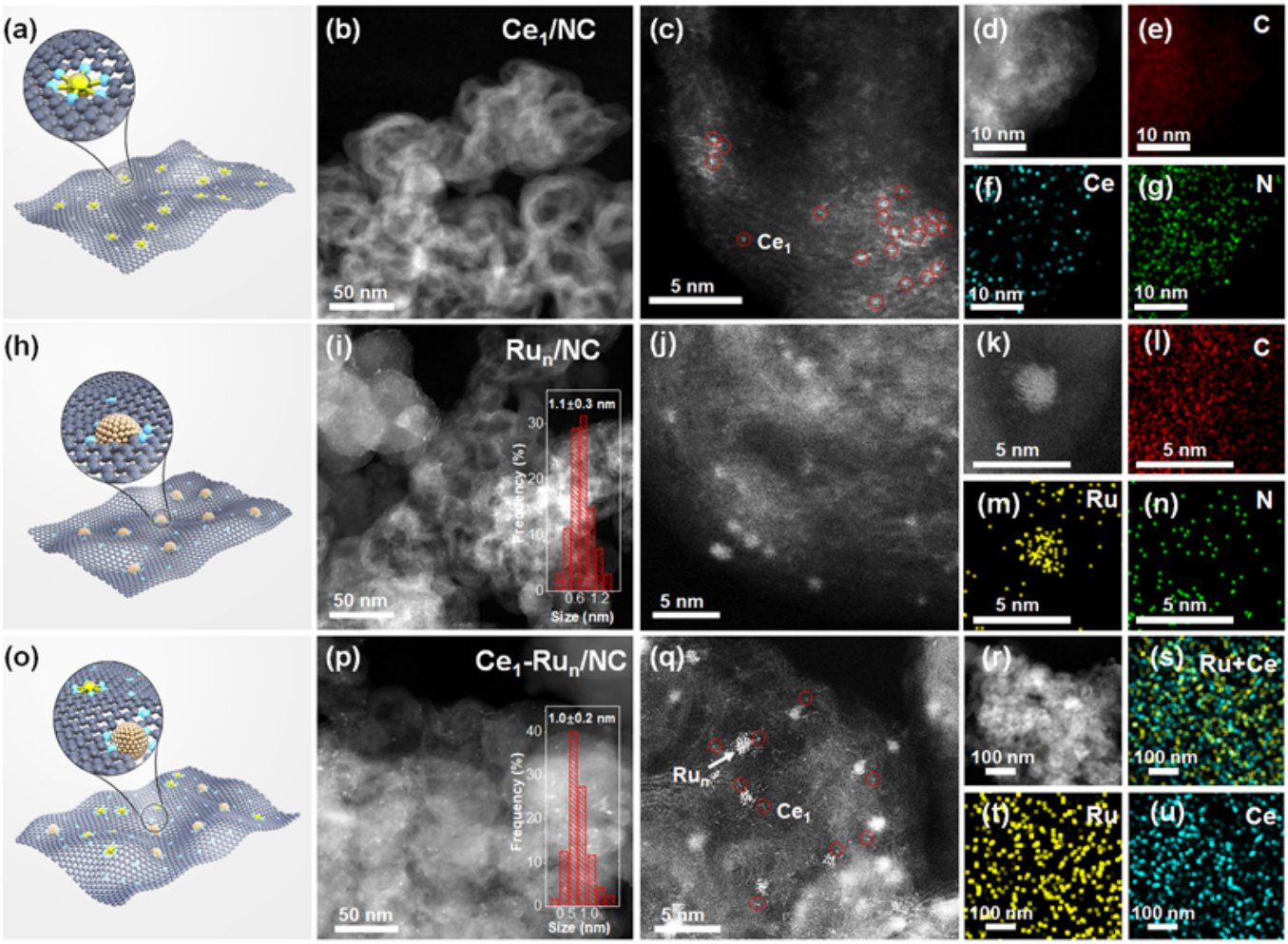

Figure 1

Microscopic measurements of the Ce_1/NC, Ru_n/NC, and Ce_1-Ru_n/NC, respectively. (a,h,o) Structural models of the Ce_1/NC, Ru_n/NC, and Ce_1-Ru_n/NC. (b)-(d) AC HAADF-STEM images, (e)-(g) EDS elementary mapping images of the Ce_1/NC. (i)-(k) AC HAADF-STEM images, (l)-(n) EDS elementary mapping images of the Ru_n/NC. (p)-(r) AC HAADF-STEM images, (s)-(u) EDS elementary mapping images of the Ce_1-Ru_n/NC. The insets of (i) and (p) are the histograms of particle-size distribution of the Ru_n/NC and the Ce_1-Ru_n/NC, respectively.

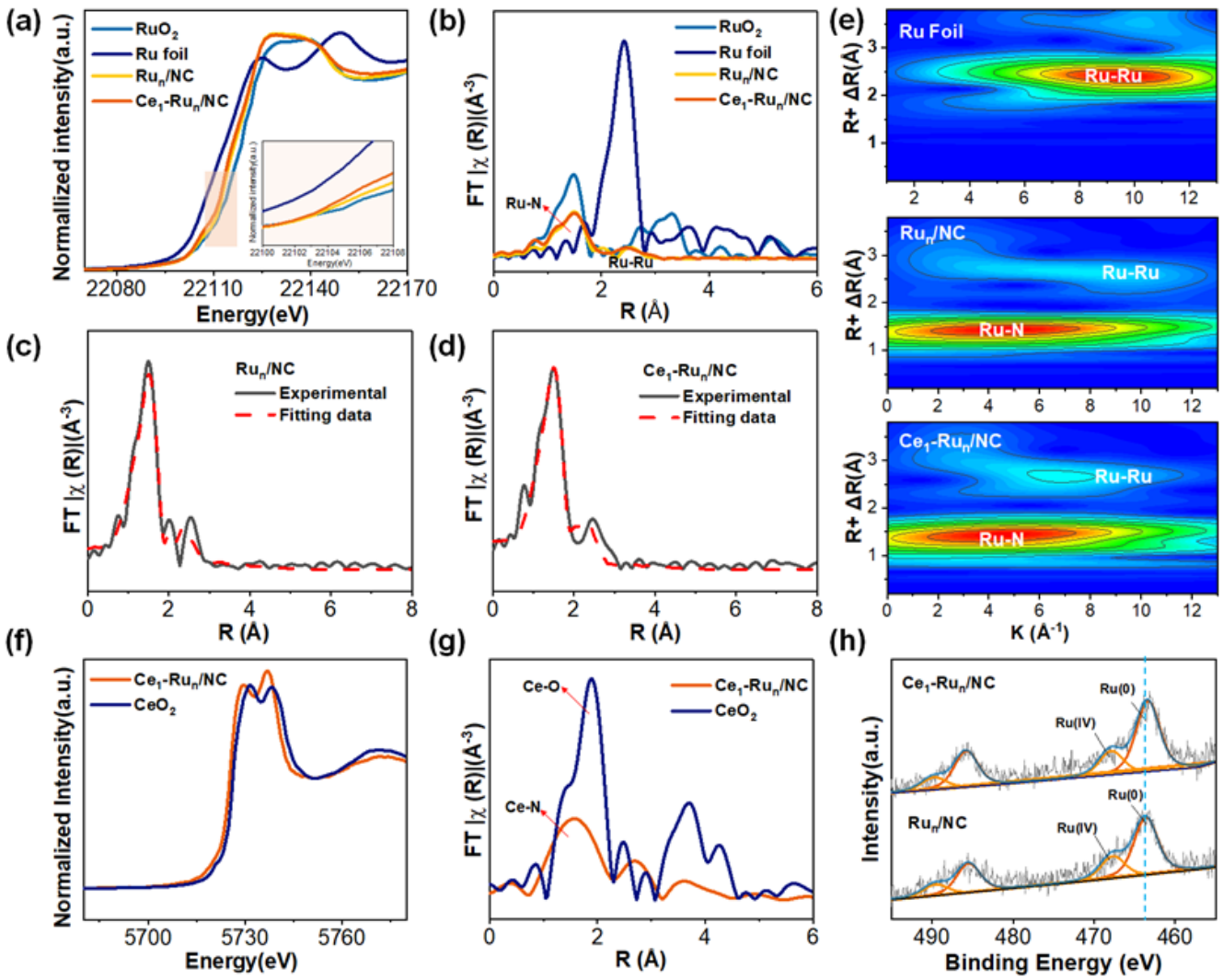

Figure 2

Characterizations of the coordination and oxidation states of the Ce_1/NC, Ru_n/NC, and Ce_1-Ru_n/NC, respectively. (a) Ru K-edge XANES spectra, (b) Fourier transforms of the Ru K-edge EXAFS oscillations in the R space of the Ce_1-Ru_n/NC, Ru_n/NC, and reference Ru foil and RuO_2. (c) and (d) EXAFS fitting curves of the Ce_1-Ru_n/NC and the Ru_n/NC. (e) Wavelet Transformation for the EXAFS signals of the Ce_1-Ru_n/NC, Ru_n/NC and Ru foil. (f) Ce L_{III}-edge XANES spectra, (g) Fourier transforms of the Ce L_{III}-edge EXAFS oscillations in the R space of the Ce_1-Ru_n/NC and the reference CeO_2. (h) Ru 3p XPS spectra of the Ce_1-Ru_n/NC and the Ru_n/NC.

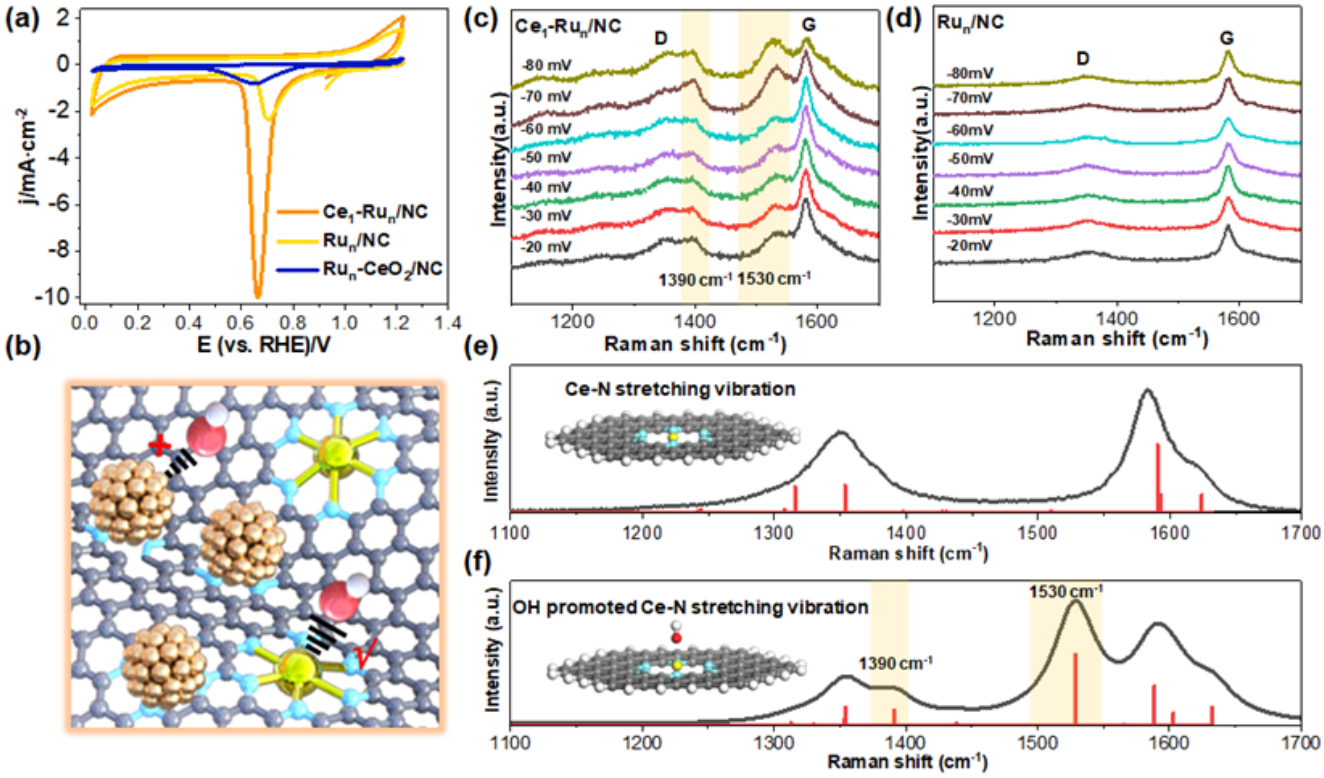

Figure 3

Exploration of the interactions between OH and the Ce_1-Ru_n/NC catalyst. (a) CV curves of the Ce_1-Ru_n/NC, Ru_n/NC, and Ru_n-CeO_2/NC catalysts measured in 1.0 M KOH solution. (b) Schematic illustration of the bonding trend between OH and Ce. *In situ* Raman spectra of the (c) Ce_1-Ru_n/NC catalyst and the (d) Ru_n/NC catalyst under real alkaline HER conditions. (e) Fitted Raman curve of the Ce-N stretching vibration in Ce_1-Ru_n/NC before alkaline HER test. (f) Fitted Raman curve of the Ce-N stretching vibration in Ce_1-Ru_n/NC in the presence of OH.

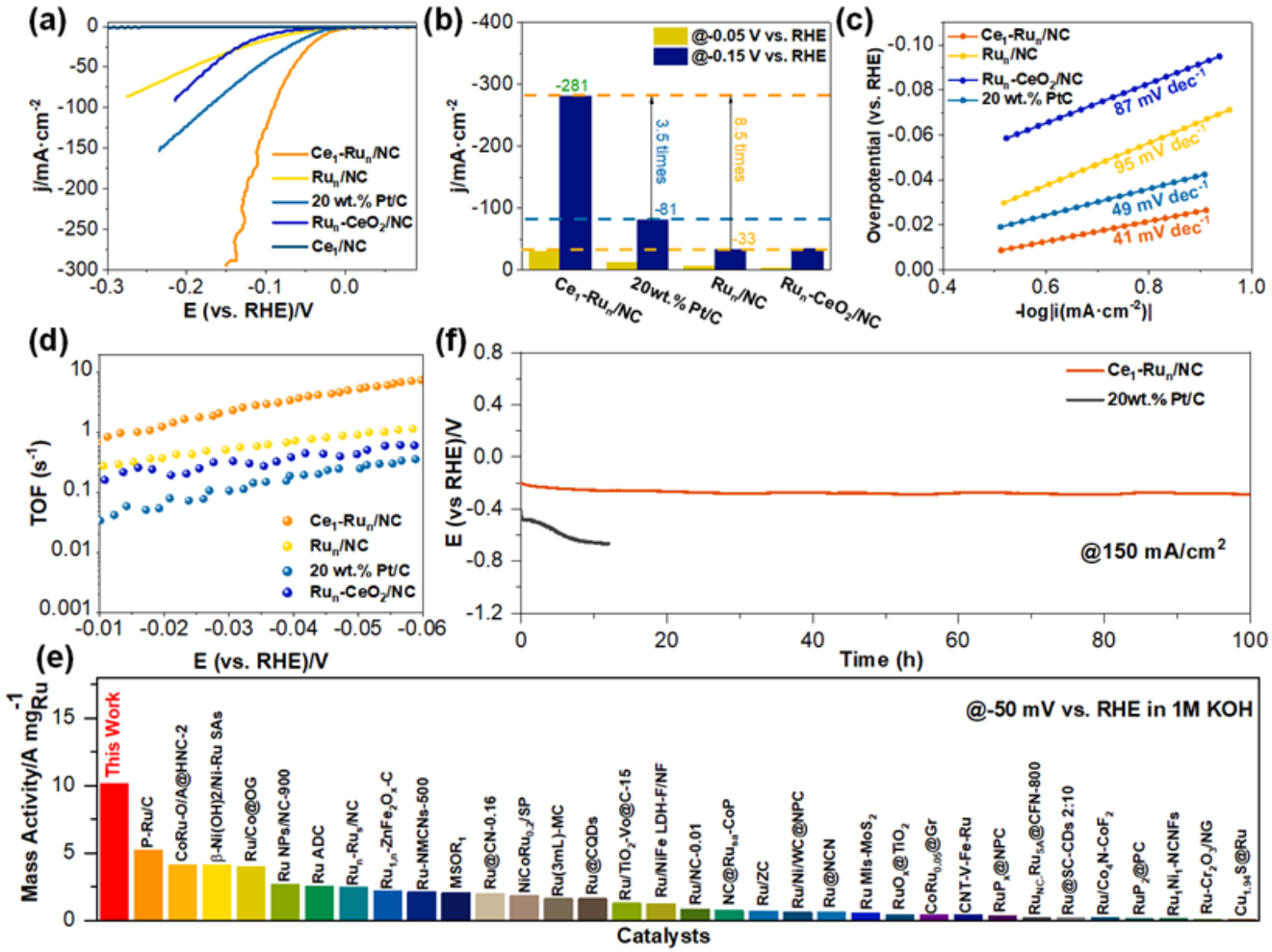

Figure 4

Electrocatalytic alkaline HER evaluations of the Ce_1-Ru_n/NC and other control catalysts. (a) LSV curves of the tested catalysts. (b) The comparison of current densities at -0.05 V and -0.15 V for the tested catalysts. (c) Tafel plots of the Ce_1-Ru_n/NC, Ru_n/NC, Ru_n-CeO_2/NC and the commercial 20wt.% Pt/C catalysts. (d) TOF values of the Ce_1-Ru_n/NC, Ru_n/NC, Ru_n-CeO_2/NC and the commercial 20wt.% Pt/C catalysts in the potential range from -0.01 V to -0.06 V. (e) Comparison of the alkaline HER mass activity of the Ce_1-Ru_n/NC with previously reported Ru-based catalysts at -0.05 V *vs.* RHE. (f) Stability test of the Ce_1-Ru_n/NC and the 20wt.% Pt/C at the current density output of 150 mA/cm^2.

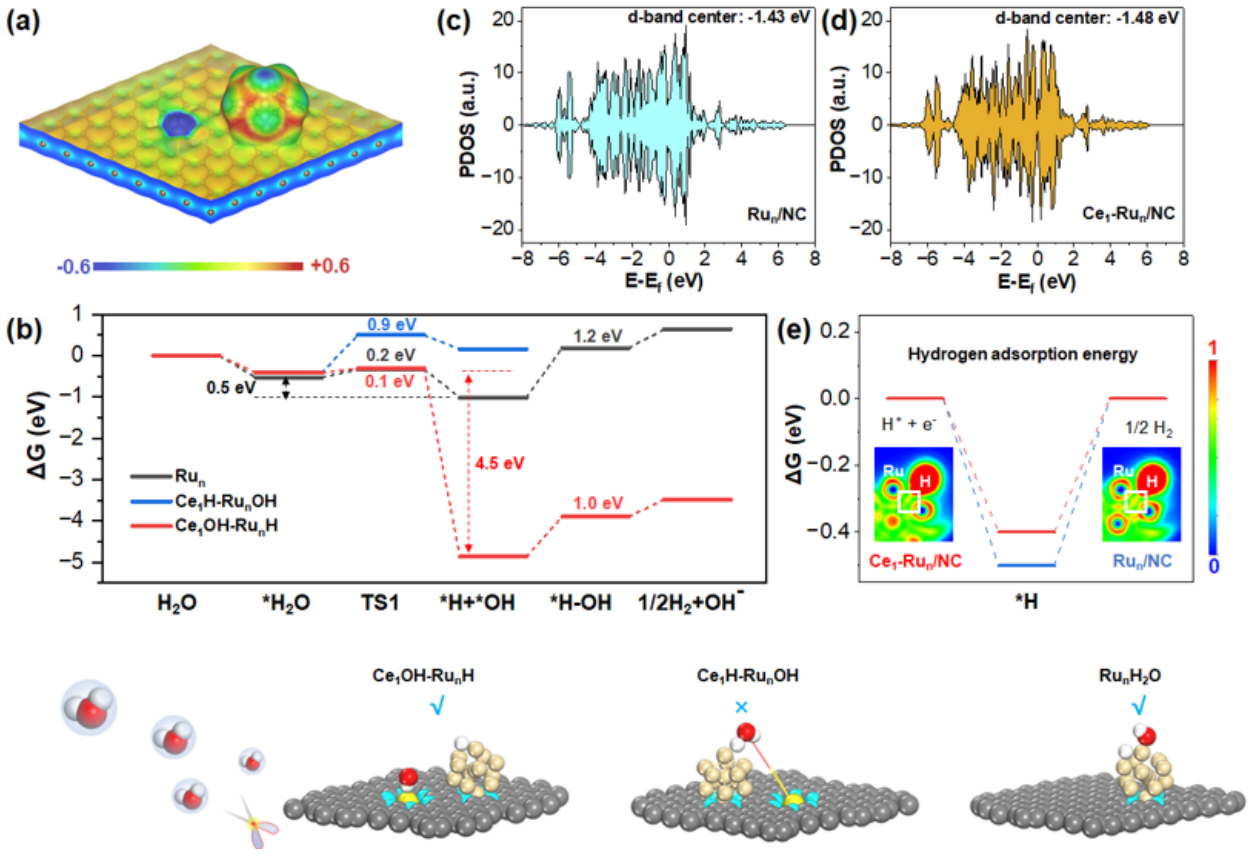

Figure 5

Reaction energy diagrams of alkaline HER over the Ce_1-Ru_n/NC and the Ru_n/NC catalysts. (a) Surface electrostatic potential distribution of the Ce_1-Ru_n/NC catalyst. (b) The Gibbs free energy diagrams for complete hydrogen evolution reaction of the Ce_1-Ru_n/NC and the Ru_n/NC catalysts in an alkaline solution. (c,d) Partial density of state (PDOS) of Ru nanoclusters for the Ce_1-Ru_n/NC and Ru_n/NC, respectively. (e) Gibbs free energy diagrams for hydrogen evolution process on Ru nanoclusters of the Ce_1-Ru_n/NC and the Ru_n/NC, respectively. The insets of (e) are the ELF pictures of *H on the Ce_1-Ru_n/NC and the Ru_n/NC, respectively.

Supplementary Files

This is a list of supplementary files associated with this preprint. Click to download.

- Supportinginformation.docx
- Scheme1.png